

A method of sharing dynamic geometry information to study liquid-based detectors*

Shu Zhang,¹ Jing-Shu Li,¹ Yang-Jie Su,^{1,2} Yu-Mei Zhang,^{3,†} Zi-Yuan Li,¹ and Zheng-Yun You^{1,‡}

¹*School of Physics, Sun Yat-Sen University, Guangzhou 510275, China*

²*School of Physical Sciences, University of Chinese Academy of Sciences, Beijing 100049, China*

³*Sino-French Institute of Nuclear Engineering and Technology, Sun Yat-Sen University, Zhuhai 519082, China*

The liquid-based detectors are widely used in particle and nuclear physics experiments. Due to the fixed way of constructing geometry in detector simulation such as Geant4, it is usually difficult to describe the non-uniformity of liquid in detectors. We propose a method based on GDML and tessellated detector description to share the detector geometry information between Computational Fluid Dynamics (CFD) simulation software and detector simulation software. The method makes it possible to study the impact of liquid flow and non-uniformity on some key performance of the liquid-based detectors, such as event vertex reconstruction resolution. It will also be helpful in detector design and performance optimization.

Keywords: liquid-based detector, geometry, simulation, Geant4, CFD

I. INTRODUCTION

In particle and nuclear physics experiments, large-scale liquid-based detectors have been widely used, especially in neutrino detectors and the experiments searching for dark matter or neutrinoless double-beta decay. For example, the Super-Kamiokande detector used 50,000 tons of ultra-pure water to detect neutrinos[1], the Sudbury Neutrino Observatory used 1,000 tons of heavy water to detect solar neutrinos[2]. In the Jiangmen Underground Neutrino Observatory (JUNO), 20,000 tons of linear alkylbenzene liquid scintillator will be used to detect the reactor neutrinos[3]. For the two future flagship neutrino experiments, Hyper-Kamiokande[4] and the Deep Underground Neutrino Experiment (DUNE)[5] will use 1 million tons of ultra-pure water and 40,000 tons of liquid argon, respectively. Besides neutrino experiments, the liquid-based detectors are also used in dark matter searches, such as the Particle and Astrophysical Xenon (PandaX) experiment[6, 7] and the Large Underground Xenon (LUX) experiment [8], which use liquid xenon in detecting dark matter candidates, as well as searching for neutrinoless nuclear double-beta decay signals.

Liquid has the advantages of high transparency, flowability, and is easy to be purified and filled into detectors, which makes it a good candidate in the design of particle and nuclear physics experiments[9, 10], especially for the large-scale experiments searching for rare signals[11] with optical processes and requiring low background environments[12].

With the liquid-based detectors designed to be bigger and bigger, a rising problem is that it becomes more and more difficult to keep the uniformity of the liquid everywhere in a huge liquid detector. Moreover, due to the flowability of liquid, the liquid flow in the detector may change the uniformity of liquid optical properties. For example, the change of refractive index due to temperature and pressure difference

may lead to deviation of optical photons transportation in the medium from the ideal uniform conditions. The impact of such deviation caused by detector non-uniformity on physical signal measurements also needs to be studied, especially in the large-scale experiments searching for rare signal events.

To study the liquid flow and non-uniformity in the detector, it is necessary to have the technique to exchange detector geometry information between different software, such as the Computational Fluid Dynamics (CFD) software and detector simulation software. A uniform detector description with detailed geometry at different parts of the liquid detector needs to be provided, and such information needs to be shared between different software with common interfaces. Since the geometry information is dynamic due to liquid flow, the transformation of detector description with the interface should be realized automatically.

We propose to develop a method based on Geometry Description Markup Language (GDML)[13] and tessellated detector description[14, 15] to share the dynamic geometry of liquid-based detectors between CFD simulation software and detector simulation software, which makes it possible to further study the extent of non-uniformity of geometry in CFD and then to study its impact on detector performance.

The structure of this paper is as follows. In Sect. 2, we will introduce the method of sharing detector geometry between software and the workflow. In Sect. 3, the method will be applied to a toy spherical detector model to study the non-uniformity of the refractive index caused by liquid flow and its influence on detector simulation and event reconstruction. In Sect. 4, the performance of the method and its further application will be discussed. Finally, the summary and conclusions will be provided in Sect. 5.

II. METHODOLOGIES

In this section, we describe the method of sharing detector geometry information between different kinds of software. With consistent detector description and automatic geometry data conversion through interfaces, the change of detector geometry can be studied in CFD simulation software, and its influence on detector performance can also be studied in de-

* Supported by the National Natural Science Foundation of China (No. 11675275, 11975021, U1932101) and the Strategic Priority Research Program of Chinese Academy of Sciences (XDA10010900).

[†] Yu-Mei Zhang zhangym26@mail.sysu.edu.cn

[‡] Zheng-Yun You youzhy5@mail.sysu.edu.cn

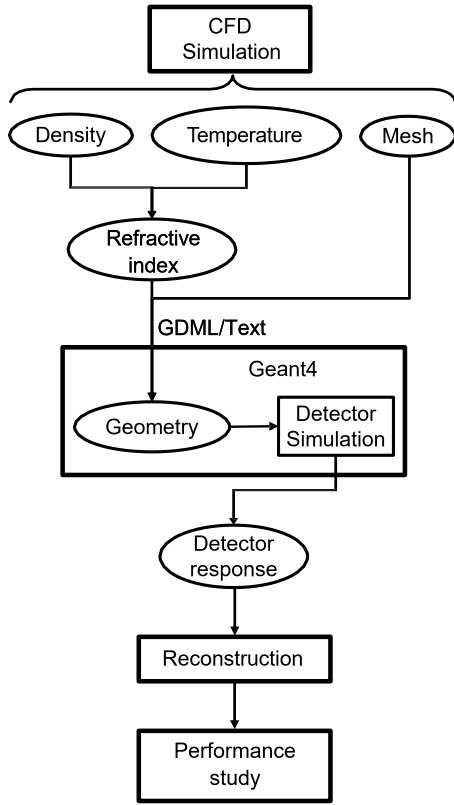


Fig. 1. Data flow of the detector geometry information from simulation to reconstruction.

tector simulation software and reconstruction software.

A typical application of the method is in the experiment using optical photons to reconstruct event vertex and energy of the physical signals, in which the density and refractive index of the liquid medium may change in different parts of the detector due to changes in temperature and pressure. Consequently, transportation of the optical photons in the medium will also change and lead to deviations in detector simulation, event reconstruction, and detector performance.

The structure of the detector geometry data flow in simulation and reconstruction with the method is shown in Fig. 1. The whole process can be divided into the following parts: CFD simulation, geometry data conversion, detector simulation, reconstruction, and detector performance study.

In this method, CFD simulation is firstly performed to study the flow of fluids in detector, with the detector geometry model being constructed and its initial conditions being set. After CFD simulation, the information of geometry mesh and fluid properties (temperature, pressure, and density distribution) are exported. Meanwhile, the related physics property of the fluid and the refractive index distribution can also be calculated and exported. The conversion of geometric information from CFD to detector simulation is realized with GDML or text format interface, including geometric mesh and fluid property information. Next, the geometry with non-uniform media properties can be built in detector simulation

software and the propagation process of the particles in the detector with non-uniform geometry can be simulated. Finally, by comparing the reconstruction results of the uniform detector simulation, the influence of the geometry change on the detector performance is evaluated.

A. CFD simulation

CFD uses numerical analysis and data structures to analyze and solve problems related to fluid flows. COMSOL Multiphysics[16] and OpenFOAM (Open-source Field Operation And Manipulation) [17] are two popular CFD simulation software that have been widely used in scientific computation.

COMSOL uses finite element analysis to decompose objects into a series of small-volume grids for calculation, in order to approximate real-world physical phenomena, especially to solve the problem of multi-physics fields coupling. In our study, the detector is first modeled and meshed, then the appropriate fluid and thermal fields are constructed, and the initial boundary conditions are set. After finite element analysis and evolution over time, the temperature, density and flow velocity distribution in each part of the detector become stable and the steady state can be obtained.

Constructing mesh of the geometric model is one of the most important steps in CFD simulation and later studies. The grid of the geometric object directly determines the solution method of the model and affects the calculation of the problem, including the solution time of the model, the amount of memory required, the interpolation method between the solution nodes, and the accuracy of the solution. The automatic mesh construction function provided by COMSOL can simplify this process, otherwise, a customized mesh needs to be built manually. Fig. 2 shows the description of a sphere with mesh and with Constructive Solid Geometry (CSG) shape, respectively.

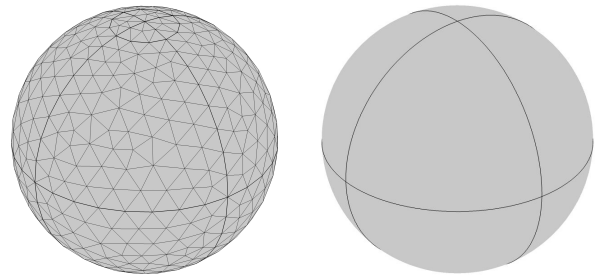


Fig. 2. Mesh geometry (left) and CSG shape (right) of a sphere.

OpenFOAM is another popular CFD simulation software. By default OpenFOAM defines a mesh of arbitrary polyhedral cells in 3D, bounded by arbitrary polygonal faces. The cells can have an unlimited number of faces and there is no limit on the number of edges nor any restriction on its alignment. This type of mesh offers great freedom in mesh generation

and manipulation, especially if the geometry of the domain is complex or changes over time. The users can also generate meshes using other packages and convert them into the format that OpenFOAM can use.

B. Geometry data conversion

In COMSOL, to construct a mesh of the geometry, the whole detector is divided into many tetrahedrons with a certain precision. The fluid property of the center point of each tetrahedron is taken as the nature of the liquid in the entire tetrahedral area. The mesh and fluid property information of each tetrahedron, including temperature, density and refractive index, need to be converted into the format that can be automatically imported into detector simulation software, such as Geant4[14], to construct the detector geometry.

In Geant4, the shape is implemented as a class `G4TessellatedSolid`, which can be used to generate a generic solid defined by several facets. With such definition, a complex geometrical shape bounded with surfaces can be converted into an approximate description with facets of defined dimension. Two types of facet can be used for the construction of a `G4TessellatedSolid`: a triangular facet and a quadrangular facet. The meshed geometry can be constructed by defining every face of the tetrahedron. Finally, all the tessellated solids form the shape of a complete detector.

There are two different ways to realize this process. One is to firstly generate a GDML file based on the geometric information exported by COMSOL, and then import the GDML file into Geant4 to construct the geometry. GDML is an XML-based[18] geometry description language used to describe the geometry of detectors in physical simulations, including their positions, rotations, shapes and materials. It is designed as an application-independent persistent format. As pure XML, GDML can be universally used as the format to interchange geometry between different applications[19]. The GDML geometry can be imported into Geant4 by the GDML parser function to construct the detector in Geant4.

GDML has been successfully applied in many HEP experiments[20], such as JUNO[21] and BESIII[22]. In JUNO, a GDML based geometry management system in JUNO offline software is designed to provide consistent detector description for different applications[23, 24]. In BESIII, the detector is described with GDML and then used in Geant4-based simulation and ROOT-based reconstruction and visualization[22].

Another method is to directly read the text format output by COMSOL in Geant4 based simulation code. A complete set of geometry information sharing interface from COMSOL to Geant4 has been developed. By using volume classes to construct solids for each tetrahedron according to its vertex coordinates and using the `G4Material` class to customize the material properties of each tetrahedron, the detector geometry with a non-uniform medium is constructed in Geant4.

C. Detector simulation

Geant4 is the most popular detector simulation software that is widely used in particle and nuclear physics experiments. The simulation process in Geant4 includes detector construction, particle transportation and interaction with materials. For a single detector component made up with a uniform material, it is usually described as a single solid volume represented by a CSG shape[25]. However, for liquid-based detectors, such approximation will lead to deviation from reality. And the level of deviation due to detector non-uniformity in large-scale detectors can be too large to be ignored, so the difference between detailed detector description and approximate uniform description needs to be studied.

To compare the impact of non-uniformity of refractive index on detector simulation, only two types of physical processes are included in detector simulation: photon propagation in a uniform medium and Fresnel refraction at the medium boundary. For the former case, the photon is regarded as a free particle and travels in a straight line throughout the whole detector. For the latter case, due to the non-uniform nature of the medium in the detector, the detector has many interfaces. The refractive index on each side of the interface is different, so the photon refracts when passing through these interfaces, and the photon path in the detector is made up of a series of steps. As an example, Fig. 3 shows the refraction of photons in the non-uniform medium.

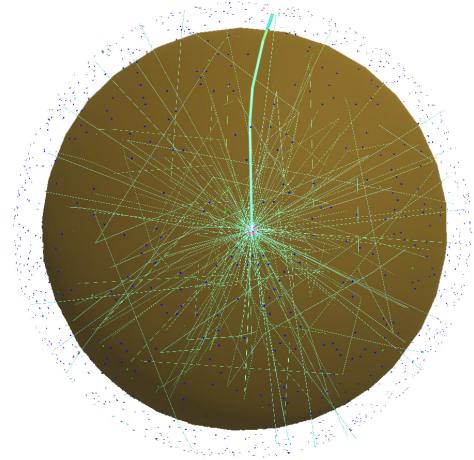


Fig. 3. Schematic of photons transportation in a spherical detector. The bold green line shows the path of a photon with multiple refractions in the non-uniform medium.

D. Detector performance study

With the output from detector simulation, the next step is to study the impact of detector description difference on detector performance. Detector performance, *e.g.*, resolution of a certain physical measurement, can be determined by analyzing detector response in simulation. The description of

detector geometry plays a key role in the simulation and in this study we test different descriptions of detector geometry for their detector performance while leaving other conditions unchanged.

III. APPLICATION

The idea of the detector geometry sharing method is originally motivated to study the optical photons transportation in liquid-based detectors. Such processes are important in many large-scale liquid-based detector experiments, especially those searching for rare signal events. For example, in neutrino experiments such as the Daya Bay reactor neutrino experiment[26], JUNO, Kamioka Liquid Scintillator anti-neutrino Detector (KamLAND)[27], Hyper-K and DUNE, optical photons from Cherenkov radiation or scintillation are used to reconstruct signal events. In dark matter search or double beta-decay experiments such as PandaX, LUX, Dark matter Experiment with Argon and Pulse-shape discrimination 3600 (DEAP-3600)[28], XENON Dark Matter Search (XENON)[29] and Depleted Argon cryogenic Scintillation and Ionization Detection (DarkSide)[30], photons or electrons also transport in the liquid detectors.

In this section, we use a toy detector model to demonstrate the feasibility of applying the method on photon transportation study. A simple spherical volume filled with water is constructed as the detector. Assuming the temperature distribution is not uniform in the spherical detector, the density of the water will be different in the detector, which makes the water flow. This step is calculated with CFD simulation software COMSOL with meshed geometry. The refractive index of the water is determined by temperature and density difference. Then the fluid properties and mesh geometry information is automatically converted to set up the geometry in Geant4 with tessellated solids.

In Geant4-based detector simulation, a virtual physical event is generated at a fixed vertex inside the sphere, and multiple photons are emitted from the vertex. The photons propagate in the water detector and finally reach the surface of the sphere. The detector simulation outputs are the hit positions of the photons on the spherical surface, which will be used to reconstruct the position of event vertex.

To study how liquid non-uniformity can affect detector performance, the detector is constructed with two methods. One is to construct a single non-uniform water sphere, the other is to construct the same water sphere with tessellated geometry, with the fluid property of each tetrahedron set from CFD simulation result. The simulation and reconstruction output will be different by using the two detector descriptions, from which the deviation and performance difference can be studied.

A. Detector mesh geometry

In CFD simulation, the radius of the sphere is set to be 15 meters and the mesh is configured to divide the sphere

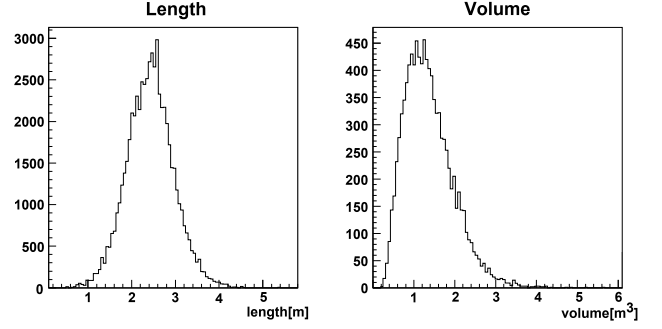


Fig. 4. Distribution of the tetrahedron side length and volume size in a meshed sphere.

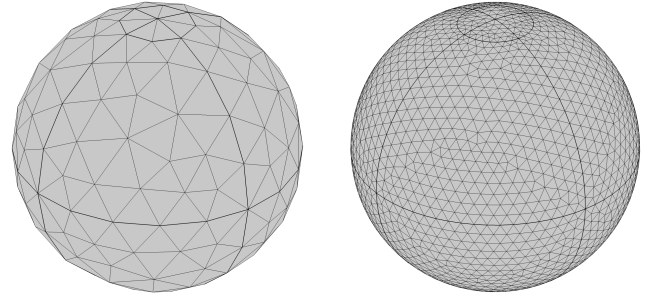


Fig. 5. Mesh geometry of the sphere with different granularity of 1,000 tetrahedrons (left) and 100,000 tetrahedrons (right).

evenly into about 10,000 tetrahedrons. Distribution of the side length and volume size of every tetrahedron is shown in Fig. 4. No tetrahedron has a particularly long side length or particularly large volume, which guarantees that the detector is evenly segmented, otherwise the properties of the medium in the tetrahedral central cannot be used to approximate the properties of the liquid in the whole tetrahedral area.

The precision of the detector description depends on the granularity of the tessellated geometry. The more tetrahedrons the sphere is divided into, the more precise the detector is described, and the more computing resource is required in CFD simulation and detector simulation. Fig. 5 shows the division of sphere into 1,000 tetrahedrons and 100,000 tetrahedrons. In Sect. 4, the dependence of vertex reconstruction deviation on the number of tetrahedrons will be studied. The correlations between the program running speed and the number of tetrahedrons will also be provided.

B. Fluid properties in CFD simulation

In CFD simulation based on COMSOL, a fixed temperature difference is set between the top and bottom of the detector as boundary conditions. To make the difference caused by temperature more significant and to test the feasibility of the method, a temperature difference of 35°C is set in a preliminary study. The correlation of performance difference with

temperature will be provided in Sect. 4.

The temperature at the top is set to be higher than the temperature at the bottom. Constant heat flux is provided in the top and bottom areas to simulate the temperature difference from the environment.

The simulation results show that when there is a temperature difference between the upper and lower surfaces of the detector, a stable temperature gradient will be formed in the medium. Fig. 6 shows the distribution of fluid temperature and flow velocity at a steady state. The temperature gradient direction is along the Z-axis and the temperature is about the same on the X-Y plane. The medium in the sphere only slowly flows horizontally on the X-Y plane, except for the area near the north and south poles.

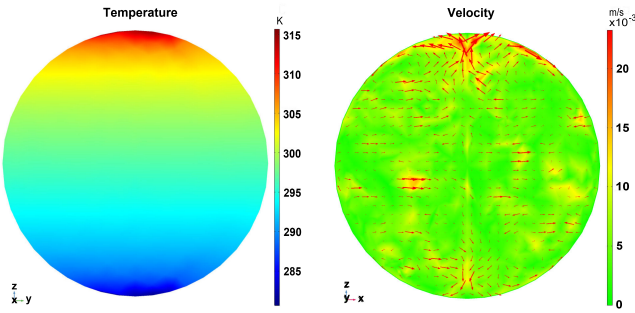


Fig. 6. Fluid temperature (left) and flow velocity (right) distribution in the spherical detector.

The refractive index of liquid is highly dependent on temperature and density. According to Ref. [31], refractive index of water in different grid of the mesh can be calculated with the following equation:

$$\frac{n^2 - 1}{(n^2 + 2)\bar{\rho}} = a_0 + a_1\bar{\rho} + a_2\bar{T} + a_3\bar{\lambda}^2\bar{T} + a_4/\bar{\lambda}^2 + \frac{a_5}{\bar{\lambda}^2 - \bar{\lambda}_{UV}^2} + \frac{a_6}{\bar{\lambda}^2 - \bar{\lambda}_{IR}^2} + a_7\bar{\rho}^2 \quad (1)$$

$$\bar{\rho} = \rho/\rho^*, \bar{T} = T/T^*, \bar{\lambda} = \lambda/\lambda^*$$

where n is the refractive index of the liquid, ρ is the density of the liquid, T is the temperature of the liquid, and λ is the wavelength of the photon. The other parameters used in the formula are shown in Table. 1.

Table 1. Parameters of the refractive index of water with wavelength, density and temperature

$a_0 = 0.244257733$	$a_4 = 1.58920570 \cdot 10^{-3}$
$a_1 = 9.74634476 \cdot 10^{-3}$	$a_5 = 2.45934259 \cdot 10^{-3}$
$a_2 = -3.73234996 \cdot 10^{-3}$	$a_6 = 0.900704920$
$a_3 = 2.68678472 \cdot 10^{-4}$	$a_7 = -1.66626219 \cdot 10^{-2}$
$\lambda_{UV} = 0.2292020$	$\lambda_{IR} = 5.432937$
$\rho^* = 1000\text{kg} \cdot \text{m}^{-3}$	$T^* = 273.15\text{K}$
$\lambda^* = 0.589\mu\text{m}$	

C. Deviation in detector simulation

The mesh of the spherical detector and its fluid properties in different grids of the mesh, including density and refractive index, will be converted into GDML format and text format that can be read by the Geant4 simulation program automatically to construct detector geometry.

To simulate a physics event at a fixed vertex inside the sphere, 1,000 optical photons are generated from the vertex isotropically in the 4π solid angle. Physically, the number of photons generated corresponds to the amplitude of the physical event, such as incident particle energy. In Geant4 simulation, the optical photons transport in the water sphere through optical processes and finally reach the surface of the sphere. Ideally, we assume that all photons can be recorded as hits at the sphere surface with 100 percent detection efficiency. These signals will be used to reconstruct the original vertex of the physics event.

To get the simulation deviation, we first simulate with the uniform medium detector to get the nominal simulation outputs. Then we run a second simulation with everything unchanged, except that the uniform sphere is replaced by the tessellated geometry describing non-uniform medium.

Fig. 7 describes the scenario with the above two geometries in detector simulation. One is to use a uniform material in detector construction, the other is to use tessellated geometry for a more precise detector description. For the optical photons crossing the neighboring tessellated volumes with different refractive indexes, only the Fresnel refraction is processed.

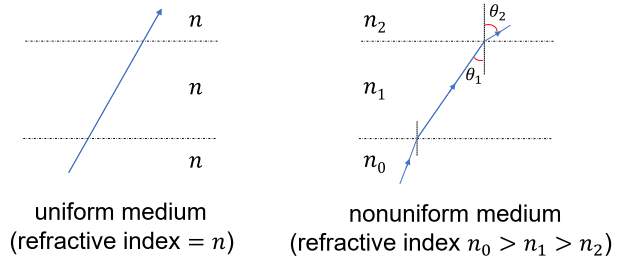


Fig. 7. Two scenarios with refraction. The left shows that photon travels in a straight line in detector described with uniform medium. The right shows that photon refracts multiple times in the detector with non-uniform medium.

The magnitude of photon momentum at the sphere surface is the same as the incident momentum, but the direction of the photon changes in each Fresnel refraction, which is described by the following equations:

$$\mathbf{p}_2 = \mathbf{p}_1 + |\mathbf{p}_1| \left(\cos \theta_1 - \frac{n_2}{n_1} \cos \theta_2 \right) \hat{\mathbf{n}} \quad (2)$$

$$\cos \theta_1 = \frac{|\mathbf{p}_1 \cdot \hat{\mathbf{n}}|}{|\mathbf{p}_1|}, \sin \theta_2 = \frac{n_1}{n_2} \sin \theta_1 \quad (3)$$

where n_1 and n_2 are the refractive index on different sides of the interface, respectively. θ_1 is the incident angle and θ_2 is

the refraction angle. p_1 is the incident momentum, p_2 is the momentum after refraction, and \hat{n} is the normalized normal vector of the refraction plane.

To get the relation of simulation deviation with event vertex, 10,000 events are simulated with vertices randomly distributed in the sphere. Each event is simulated twice with the two different detector descriptions to get the deviation. Then we can compare the photon hit positions on the detector surface due to refraction caused by medium non-uniformity.

A comparison of the results from two simulations shows that the hit position on the detector surface is significantly shifted under the preliminary conditions. The deviation is at mm level. Fig. 8 shows the distribution of the magnitude and direction of the deviation on the sphere surface. The magnitude of deviation has no obvious relationship with the hit position on the sphere. Most of the photon positions on the sphere surface deflect toward the negative Z-axis in simulation with the non-uniform detector, no matter the original direction of the photon from vertex points upward or downward. It is because the temperature increases along the positive Z-axis direction and the refractive index decreases along the positive Z-axis direction, as shown in Fig. 6.

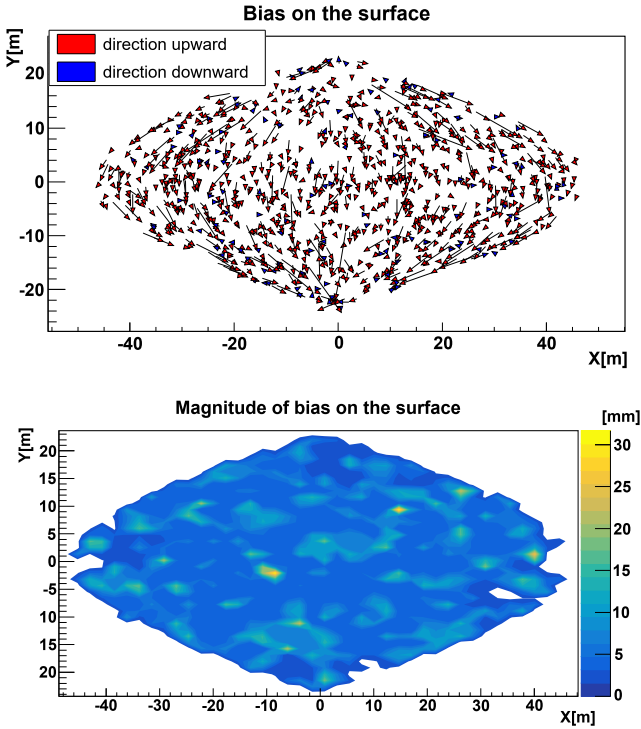


Fig. 8. Distribution of the magnitude and direction of the deviation on the detector surface (top). The blue and red arrows indicate the offset direction along the positive Z-axis and negative Z-axis direction, respectively. The length of the arrow indicates the relative magnitude of the deviation. A 2D projection of the magnitude of the offset on the sphere surface is also shown (bottom).

Fig. 9 shows the distribution of the deviation angle offset on longitude (θ) and latitude (α) direction, which are defined in the schematic view of the sphere in Fig. 10. Since the temperature on the same Z plane is the same, there is no significant

trend that the photon hits with the same Z on the surface deflect to the left or right systematically.

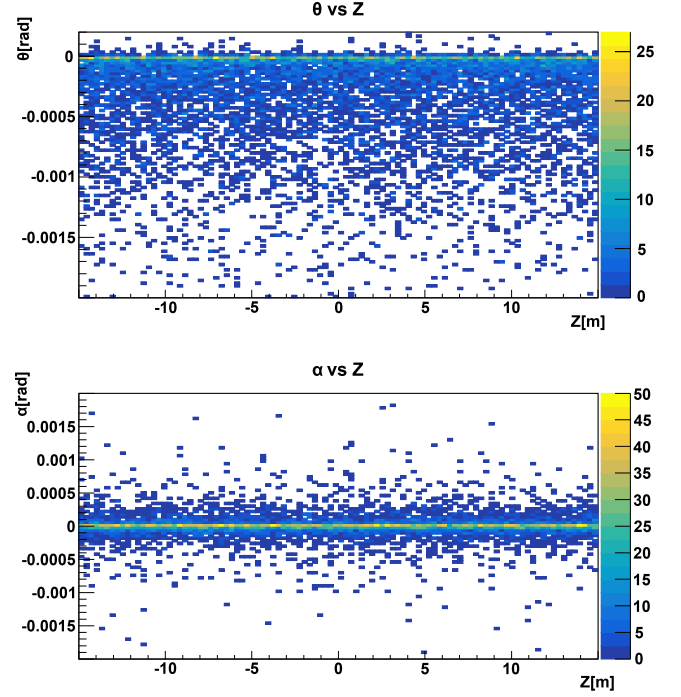


Fig. 9. Distribution of the deviation angle θ (top) and α (bottom) with the Z coordinate.

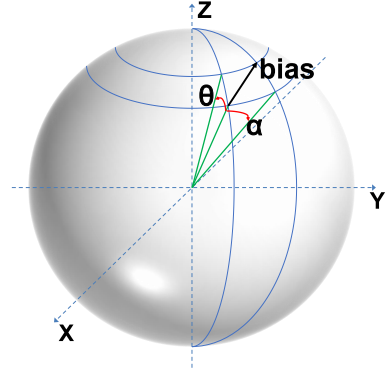


Fig. 10. Schematic view of the deviation angle on sphere surface. θ and α represent the deviation angle component along the longitude and latitude direction, respectively.

D. Deviation in vertex reconstruction

In most experiments, the event vertex position, which shows where the physics event is generated, is an important physics quantity to measure. The vertex position resolution is a key indicator to evaluate the detector performance. To study the effect of the non-uniformity of the medium properties on detector vertex position resolution, the charge-weighted algo-

rithm is used to reconstruct event vertex from the photons' hit position on the sphere surface.

Fig. 11 shows the principle of the charge-weighted algorithm. Assuming that the true event vertex is located at the position $Z = z_0$ and there are n photons emitted from the vertex, whose momentum directions are isotopically distributed in the 4π solid angle of the vertex, the average value of the z component of the hit position of all photons on the sphere is:

$$\begin{aligned}\bar{z} &= \frac{1}{4\pi} \int z d\Omega \\ &= \frac{1}{4\pi} \int_0^{2\pi} d\phi \int_0^\pi (z_0 + r \cos \theta) \sin \theta d\theta \\ &= \frac{2}{3} z_0\end{aligned}\quad (4)$$

Then the reconstructed event vertex \bar{V} can be obtained as:

$$\bar{V} = \frac{3}{2n} \sum_i V_i \quad (5)$$

where n is the total number of photons and V_i is the hit position of the i -th photon on the sphere.

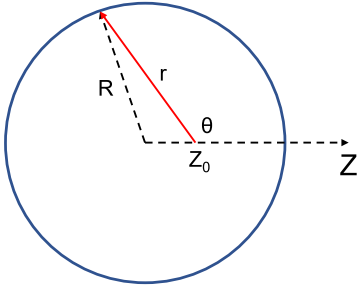


Fig. 11. Sketch of the charge-weighted algorithm for vertex reconstruction.

To compare the event vertex reconstruction deviation, we simulate 10,000 events. Each event is simulated twice, with uniform and with non-uniform detector geometry, respectively. The two simulation results are reconstructed with the same charge-weighted algorithm, then we compare the two reconstructed vertices to get the deviation in this event due to the geometry difference. Fig. 12 shows the distribution of reconstructed vertex deviation for the 10,000 events. The deviations due to geometry difference are at a few mm level with a long tail up to 80 mm. The average deviation is about 10 mm. Although the charge-weighted algorithm has a vertex reconstruction resolution itself, in the two simulations of every single event, every original condition is the same except the detector geometry. So the comparison is between the two reconstructed vertices rather than their respective bias from the true vertex.

In this section, we use a set of fixed-parameter (sphere radius = 15m, temperature difference = 35°C, and the sphere mesh number = 10,000) to get a preliminary result to show the feasibility of applying the geometry sharing method on liquid-based detector simulation, reconstruction and get the deviation distribution.

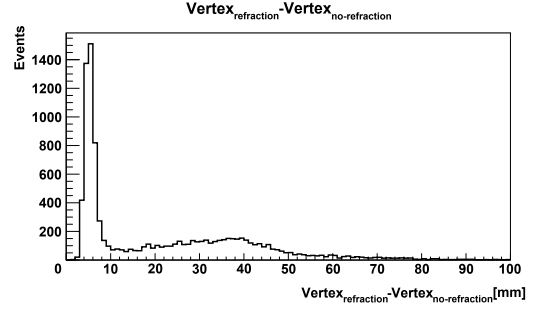


Fig. 12. The vertex reconstruction deviation due to geometry difference.

IV. COMPARISON

To study the influence of different conditional parameters on the detector performance, we change the size of the detector, the temperature difference, and the mesh granularity to check the consequential changes on simulation and vertex reconstruction results.

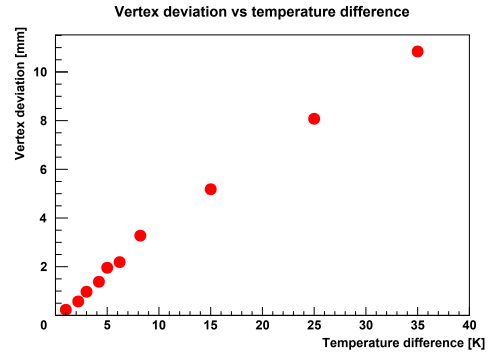


Fig. 13. The average deviation of the reconstructed vertex changes with the temperature difference.

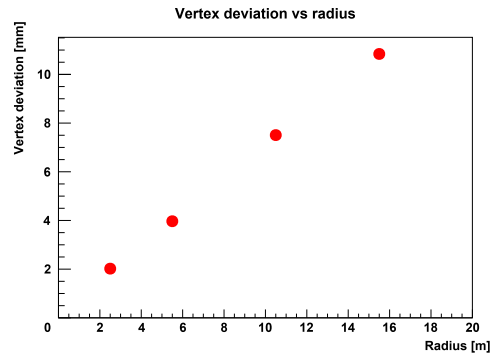


Fig. 14. The average deviation of the reconstructed vertex changes with the radius of the sphere.

In real conditions of an experiment, the environment temperature could be different. Usually, the temperature difference is at a few Celsius degree level. The higher it is, the

more significant its impact on detector performance will be. Fig. 13 shows that the reconstructed vertex deviation is linearly dependent on the temperature difference. Fig. 14 shows that the reconstructed vertex deviation is linear with the size of the detector. These conclusions are expectable since the method itself is size-independent.

Fig. 15 shows the dependency of vertex reconstruction deviation on the mesh granularity, *i.e.*, the number of tetrahedrons that a sphere is segmented into. When the segmentation is very coarse, deviations of the reconstructed vertex gradually increase with the improvement of the segmentation accuracy. After the number of tetrahedrons reaches 5,000, the deviation level becomes stable. To determine the granularity of detector segmentation, it is necessary to comprehensively consider the available computing resources and the result accuracy requirements.

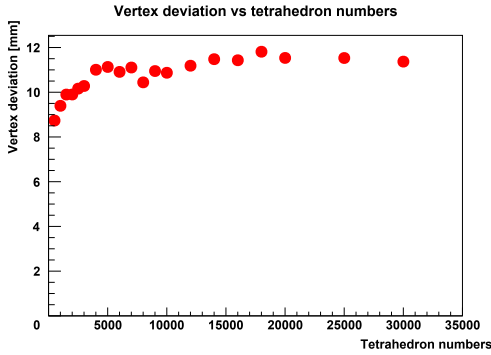


Fig. 15. The average deviation of the reconstructed vertex changes with the segmentation accuracy.

Fig. 16 shows the deviation dependency on the heat flux area angle. When the heat flux area is close to the top or bottom of the sphere, the deviation of the reconstruction vertex is little affected by the heat flux location change, but when the location deviates greatly from the Z-axis by nearly 90 degrees, the deviation of the reconstructed vertex is significantly reduced.

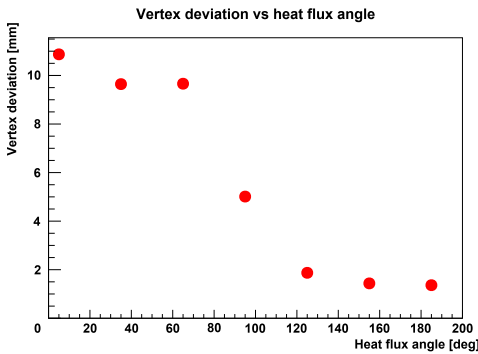


Fig. 16. The average deviation of the reconstructed vertex changes with the heat flux area angle.

The reason for the influence of the location of the heat flux area is that the formation of the temperature gradient has

a strong correlation with the location of the heat flux area. Fig. 17 shows the temperature distribution that reaches stable when the heat flux region deviates from the Z-axis by 30 degrees and by 150 degrees, respectively, in which the red and blue areas on the surface represent hot and cold areas where heat flux exists. When the heat flux area deviates from the Z-axis by 30 degrees, the medium heated in the hot area rises along the ball wall to the top and decelerates, and then flows back to the hot area along the horizontal ball wall. The case is similar in the cold area. Therefore, the liquid in the sphere has almost no vertical flow but mainly horizontal flow.

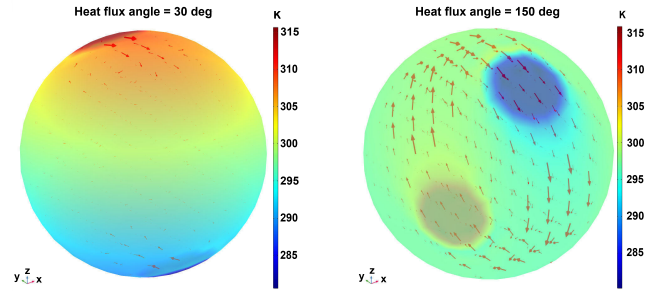


Fig. 17. The distributions of temperature and liquid flow in the sphere when the CFD simulation reaches stable, for the two cases when the heat flux area deviates from the Z-axis by 30 degrees (left) and by 150 degrees (right), respectively.

Since there is only local circulation, when the heat flux area deviates from the Z-axis by an angle that is not too large, a temperature gradient similar to the case when the heat flux area is on the Z-axis can still be formed. When the heat flux area deviates far from the Z-axis, the temperature difference between the upper and lower endpoints along the temperature gradient direction in the stable state becomes smaller.

Fig. 18 shows the temperature distribution along the Z-axis at a steady state. When the temperature difference of the heat flux is 35 K and the heat flux location deviates from the Z-axis by 60 degrees, the temperature difference is comparable to the case when the temperature difference of the heat flux is 15 K and the position is along the Z-axis, but the temperature gradient of the former is greater. However, when the heat flux area deviates from the Z-axis by more than 90 degrees (Fig. 17 right), the heated liquid flows upwards from the hot area, when it reaches the cold area on the top, the liquid is quickly cooled and sinks. Therefore it forms an annular flow in the sphere and no obvious temperature gradient can be formed due to the circulation.

Computing resources consumption is also compared in the study. When the number of tetrahedrons increases with the improvement of segmentation accuracy, it takes more CPU time in COMSOL and Geant4 simulation. The simulation time with different numbers of tetrahedrons is listed in Table. 2, which is the CPU time for COMSOL to simulate fluid flow for 5 hours clock time and for Geant4 to simulate 100,000 particles. The CPU time used by the two geometry data conversion methods of text format and GDML is also compared. In Geant4 simulation, it takes more time to import

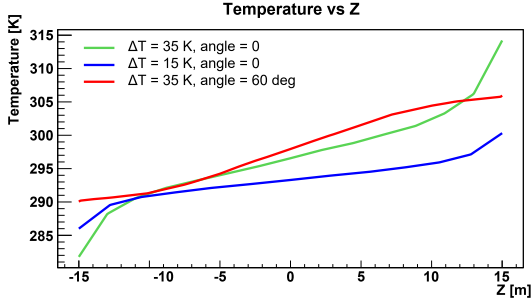


Fig. 18. The temperature distribution in the sphere along the Z-axis with different ΔT and different heat flux angle.

the geometry through the GDML file than directly reading the text file to construct the geometry. With the segmentation accuracy increased, the computing speed difference between the two methods becomes more obvious.

Table 2. CPU time consumption for each part of simulation

tetrahedron numbers	Geant4			COMSOL
	Geometry initialization		simulation	
	Text	GDML		
1,000	<1s	8s	27s	21min
10,000	2s	13s	58s	137min
30,000	7s	44s	85s	321min

V. DISCUSSION

In this method, the generation of correct geometry mesh is an important step. The entire detector must be fully segmented, otherwise, the properties of the tetrahedral central medium cannot be used to approximate the properties of the entire tetrahedron. In this study, only the method of global automatic segmentation is adopted, and only the tetrahedron segmentation is considered.

At the same time, the influence of medium non-uniformity

will reach saturation with the improvement of the segmentation accuracy. Too high segmentation accuracy does not help much on simulation and reconstruction precision, but will greatly increase the CPU time consumption in CFD simulation and Geant4 simulation. In more realistic detector simulations, more complicated physical processes, more particles, and more complicated environments will be usually introduced, which may further increase the simulation time.

GDML and text format are both used for geometry data sharing from COMSOL to Geant4. Creating geometry by directly reading text files is much faster than importing GDML files into Geant4 to initialize geometry. However, GDML is widely used in Geant4 simulation and reconstruction based on ROOT[32] geometry package, which can provide consistent geometric information for subsequent data analysis.

In our research, it is assumed that the hot area is on the top and the cold area is at the bottom, so that the temperature gradient can be formed. When the location of the hot area is lower than the cold area, due to the formation of convection and circulation in the sphere, the temperature in the sphere is almost the same and no temperature gradient can be formed. The whole spherical detector may be considered to be uniform and no obvious deviations in simulation and reconstruction will be observed.

VI. CONCLUSION

A method of dynamic geometry information sharing between CFD simulation and detector simulation is proposed for liquid-based detectors. Its feasibility is demonstrated by the application of the method to simulate with non-uniform medium to study photon transportation and event vertex reconstruction deviation. This method can also be used to study other dynamic geometry related problems in particle and nuclear physics experiments, such as the expansion and contraction of the detector volumes due to temperature change, detector alignment at different running periods of the experiments, and geometry related magnetic field changes.

-
- [1] K. Abe, et al., Evidence for the Appearance of Atmospheric Tau Neutrinos in Super-Kamiokande. *Phys. Rev. Lett.* 110, 181802 (2013). doi: [10.1103/PhysRevLett.110.181802](https://doi.org/10.1103/PhysRevLett.110.181802)
 - [2] Q. Ahmad, et al., Direct Evidence for Neutrino Flavor Transformation from Neutral-Current Interactions in the Sudbury Neutrino Observatory. *Phys. Rev. Lett.* 89, 011301 (2002). doi: [10.1103/PhysRevLett.89.011301](https://doi.org/10.1103/PhysRevLett.89.011301)
 - [3] T. Adam, et al., JUNO Conceptual Design Report (2015). [arXiv:1508.07166](https://arxiv.org/abs/1508.07166)
 - [4] K. Abe, et al., Hyper-Kamiokande Design Report (2018). [arXiv:1805.04163](https://arxiv.org/abs/1805.04163)
 - [5] R. Acciarri, et al., Long-Baseline Neutrino Facility (LBNF) and Deep Underground Neutrino Experiment (DUNE) Conceptual Design Report, Volume 4 The DUNE Detectors at LBNF (2016). [arXiv:1601.02984](https://arxiv.org/abs/1601.02984)
 - [6] X. Cao, X. Chen, Y. Chen, et al., PandaX: a liquid xenon dark matter experiment at CJPL. *Sci. China Phys. Mech. Astron.* 57, 1476-1494 (2014). doi: [10.1007/s11433-014-5521-2](https://doi.org/10.1007/s11433-014-5521-2)
 - [7] H. Zhang, et al., Dark matter direct search sensitivity of the PandaX-4T experiment. *Sci. China Phys. Mech. Astron.* 62, 31011 (2019). doi: [10.1007/s11433-018-9259-0](https://doi.org/10.1007/s11433-018-9259-0)
 - [8] D.S. Akerib, et al., Results from a Search for Dark Matter in the Complete LUX Exposure. *Phys. Rev. Lett.* 118, 021303 (2017). doi: [10.1103/PhysRevLett.118.021303](https://doi.org/10.1103/PhysRevLett.118.021303)
 - [9] P. Juyal, K.L. Giboni, X.D. Ji, et al., On proportional scintillation in very large liquid xenon detectors. *Nucl. Sci. Tech.* 31, 93 (2020). doi: [10.1007/s41365-020-00797-4](https://doi.org/10.1007/s41365-020-00797-4)
 - [10] M.Y. Huang, H. Pei, X.M. Sun, et al., Simulation study of energy resolution with changing pixel size for radon monitor based on *Topmetal-II* TPC. *Nucl. Sci. Tech.* 30, 16 (2019).

- doi: [10.1007/s41365-018-0532-8](https://doi.org/10.1007/s41365-018-0532-8)
- [11] Y.L. Yan, W.X. Zhong, S.T. Lin, et al., Study on cosmogenic radioactive production in germanium as a background for future rare event search experiments. *Nucl. Sci. Tech.* 31, 55 (2020). doi: [10.1007/s41365-020-00762-1](https://doi.org/10.1007/s41365-020-00762-1)
 - [12] K.L. Giboni, P. Juyal, E. Aprile, et al., A LN₂-based cooling system for a next-generation liquid xenon dark matter detector. *Nucl. Sci. Tech.* 31, 76 (2020). doi: [10.1007/s41365-020-00786-7](https://doi.org/10.1007/s41365-020-00786-7)
 - [13] R. Chytrcek, et al., Geometry Description Markup Language for Physics Simulation and Analysis Applications. *IEEE Trans. Nucl. Sci.* 53, 881062 (2006). doi: [10.1109/TNS.2006.881062](https://doi.org/10.1109/TNS.2006.881062)
 - [14] S. Agostinelli, et al., GEANT4—a simulation toolkit. *Nucl. Instrum. Meth. A.* 506, 250-303 (2003). doi: [10.1016/S0168-9002\(03\)01368-8](https://doi.org/10.1016/S0168-9002(03)01368-8)
 - [15] J. Allison, et al., Geant4 developments and applications. *IEEE Trans. Nucl. Sci.* 53, 869826 (2006). doi: [10.1109/TNS.2006.869826](https://doi.org/10.1109/TNS.2006.869826)
 - [16] COMSOL Multiphysics, Introduction to COMSOL multiphysics. COMSOL Multiphysics (2016). <https://www.comsol.com>
 - [17] H. Jasak, A. Jemcov, Z. Tukovic, Openfoam: A C++ library for complex physics simulations. International Workshop on Coupled Methods in Numerical Dynamics, Dubrovnik, Croatia, 1-20 (2007). <http://cmnd2007.fsb.hr>
 - [18] T. Bray, J. Paoli, C. Sperberg-McQueen, Extensible Markup Language (XML) 1.0. <http://www.w3.org/XML/1998/06/xmlspec-report-19980910.htm>
 - [19] X. Wang, J.L. Li, Z. Wu, et al., CMGC: a CAD to Monte Carlo geometry conversion code. *Nucl. Sci. Tech.* 31, 82 (2020). doi: [10.1007/s41365-020-00793-8](https://doi.org/10.1007/s41365-020-00793-8)
 - [20] Z. You, et al., A method for detector description exchange among ROOT GEANT4 and GEANT3, *Chin. Phys. C.* 32, 572 (2008). doi: [10.1088/1674-1137/32/7/012](https://doi.org/10.1088/1674-1137/32/7/012)
 - [21] K. Li, et al., GDML based geometry management system for offline software in JUNO. *Nucl. Instrum. Meth. A.* 908, 43-48 (2018). doi: [10.1016/j.nima.2018.08.008](https://doi.org/10.1016/j.nima.2018.08.008)
 - [22] Y. Liang, et al., A uniform geometry description for simulation, reconstruction and visualization in the BESIII experiment. *Nucl. Instrum. Meth. A.* 603, 325-327 (2009). doi: [10.1016/j.nima.2009.02.036](https://doi.org/10.1016/j.nima.2009.02.036)
 - [23] Z. You, et al., A ROOT based event display software for JUNO. *JINST.* 13, T02002 (2018). doi: [10.1088/1748-0221/13/02/T02002](https://doi.org/10.1088/1748-0221/13/02/T02002)
 - [24] J. Zhu, et al., A method of detector and event visualization with Unity in JUNO. *JINST.* 14, T01007 (2019). doi: [10.1088/1748-0221/14/01/T01007](https://doi.org/10.1088/1748-0221/14/01/T01007)
 - [25] H. Dong, D.Q. Fang, C. Li, Study on the performance of a large-size CsI detector for high energy γ -rays. *Nucl. Sci. Tech.* 29, 7 (2018). doi: [10.1007/s41365-017-0345-1](https://doi.org/10.1007/s41365-017-0345-1)
 - [26] F.P. An, et al., Improved measurement of electron antineutrino disappearance at Daya Bay. *Chin. Phys. C.* 37, 011001 (2013). doi: [10.1088/1674-1137/37/1/011001](https://doi.org/10.1088/1674-1137/37/1/011001)
 - [27] S. Abe, et al., Production of radioactive isotopes through cosmic muon spallation in KamLAND. *Phys. Rev. C.* 81, 025807 (2010). doi: [10.1103/PhysRevC.81.025807](https://doi.org/10.1103/PhysRevC.81.025807)
 - [28] P.A. Amaudruz, et al., Design and construction of the DEAP-3600 dark matter detector. *Astropart. Phys.* 108, 1-23 (2019). doi: [10.1016/j.astropartphys.2018.09.006](https://doi.org/10.1016/j.astropartphys.2018.09.006)
 - [29] E. Aprile, et al., Light dark matter search with ionization signals in XENON1T. *Phys. Rev. Lett.* 123, 251801 (2019). doi: [10.1103/PhysRevLett.123.251801](https://doi.org/10.1103/PhysRevLett.123.251801)
 - [30] P. Agnes, et al., Low-Mass Dark Matter Search with the DarkSide-50 Experiment. *Phys. Rev. Lett.* 121, 081307 (2018). doi: [10.1103/PhysRevLett.121.081307](https://doi.org/10.1103/PhysRevLett.121.081307)
 - [31] P. Schiebener, et al., Refractive index of water and steam as function of wavelength, temperature and density. *J. Phys. Chem. Ref. Data* 19, 677 (1990). doi: [10.1063/1.555859](https://doi.org/10.1063/1.555859)
 - [32] R. Brun, F. Rademakers, ROOT - An object oriented data analysis framework. *Nucl. Instrum. Meth. A.* 389, S0168 (1997). doi: [10.1016/S0168-9002\(97\)00048-X](https://doi.org/10.1016/S0168-9002(97)00048-X)